Nanoscale Analysis of the Structure and Composition of Biogenic Calcite Reveals the Biomineral Growth Pattern

Marta de Frutos, Alejandro Rodríguez-Navarro, Xiaoyan Li, Antonio Checa

NANOSCALE ANALYSIS OF THE STRUCTURE AND COMPOSITION OF BIOGENIC CALCITE REVEALS THE BIOMINERAL GROWTH PATTERN

Marta de Frutos[a], Alejandro B. Rodríguez-Navarro[b], Xiaoyan Li[a], Antonio G. Checa[c]*

[a] Laboratoire de Physique des Solides (LPS), CNRS UMR 8502, Université Paris-Saclay, F-91405, Orsay, France.

[b] Departamento de Mineralogía y Petrología, Universidad de Granada, ES-18071 Granada, Spain.

[c] Departamento de Estratigrafía y Paleontología, Universidad de Granada, ES-18071 Granada, Spain, and Instituto Andaluz de Ciencias de la Tierra, CSIC-Universidad de Granada, 18100 Armilla, Spain.

* Marta de Frutos

Email: marta.de-frutos@universite-paris-saclay.fr

Abstract

The vast majority of calcium carbonate biocrystals differ from inorganic crystals in that they display a patent nanoroughness consisting of lumps of crystalline material (calcite/aragonite) surrounded by amorphous pellicles. Scanning transmission electron microscopy coupled with electron energy loss spectroscopy (STEM-EELS) was used to map the calcite secreted by a barnacle chemically and structurally with ultra-high resolution (down to 1 nm). The material is composed of irregular lumps of calcite (up to two hundred nm in diameter) surrounded by relatively continuous cortexes (up to 20 nm thick) of amorphous calcium carbonate (ACC) and/or nanocalcite plus biomolecules, with a surplus of calcium relative to carbonate. We develop a model by which the separation of the crystalline and amorphous phases takes place upon crystallization of the calcite from a precursor ACC. The organic biomolecules are expelled from the crystal lattice and concentrate in the form of pellicles, where they stabilize minor amounts of ACC/nanocalcite. In this way, we change the previously established conception of biomineral structure and growth.

Keywords: biogenic calcite, nanostructure, amorphous precursors, shell biomineralization, STEM-EELS

The minerals secreted by organisms are remarkable in many respects but particularly because of their high degree of sophistication, with shapes and relationships far from those found in the inorganic world. Since the turn of the millennium, several studies have revealed that they are also unique in terms of their nanostructures. In the last 20 years it has become more and more patent that the calcium carbonate minerals (biocalcite and bioaragonite) produced by most organisms, particularly metazoans, show a marked surface roughness at the nanoscale. Nanoroughness consists of protrusions with sizes ranging from a few to a few hundreds of nm. These differently sized nanoprotrusions intermingle in a quasi-fractal mode[1]. In the literature, this feature has been referred to as nanoparticulate, nanogranular, nanoglobular or nanopatterned. Although the initial observations were carried out with scanning electron microscopy (SEM) in the 70s[2,3] it was not until the early 2000s that the introduction of the atomic force microscopy (AFM), with its high resolution, provided a clearer picture of the surface nanoroughness of biominerals[4,5] This feature was amply revealed in molluscs[4–9] calcareous sponges[10], corals[11], echinoderms[12], cirripeds[1], brachiopods[13], bryozoans (unpublished observations), fish otoliths[14], and avian eggshells[15]. Hitherto, the only biominerals found not to display this kind of surface roughness are coccoliths[16,17]. Accordingly, the surface nanoroughness quality is widely used as a diagnostic feature for biominerals[18,19]. Specifically, AFM phase imaging revealed the presence of two phases with different contrast: (1) a low contrast phase, which makes up the bulk of the material and shows the surface nanoroughness, and (2) a high contrast (noticeably darker) minority phase that distributes as nanometer-thick pellicles around and between the protrusions. Observations on polished and fractured specimens revealed that the two phases distribute also within the interior of the crystals[1,4,6,8,11,20–23], providing a 'foamy' aspect, with the dark phase corresponding to the liquid and the light phase, to the air in a foam. The dark phase is not a continuous phase and leaves gaps through which the lumps of the light phase connect with each other[6,24]. There is consensus

that the light majority phase is the crystalline phase (calcite or aragonite), and the discussion is mainly on the nature of the high contrast phase. Based only on AFM evidence, some authors attributed to this phase an organic[4,5,7,8,21,23,24], and/or amorphous calcium carbonate (ACC) composition[6,22] and suggest that the organic/crystalline distribution is responsible for this nanostructure. De Vol et al. (ref. 41) found ACC in incipient nacre platelets with photoemission electron spectromicroscopy (PEEM) but the resolution (20 nm) and the absence of information concerning the organic fraction did not allow for the attribution of a particular composition to any of the phases recognized with AFM.

The only reliable data were obtained with the help of transmission electron microscopy (TEM). Nassif et al.[25] observed amorphous rims around nacre tablets, that upon beam exposure, recrystallized into aragonite, making them assume a merely ACC composition. Thin (~4 nm wide) and elongated amorphous areas were observed by Seto et al.[12] in the interior of the calcitic sea urchin spine. Supported by etching experiments, they attributed these areas to ACC and macromolecules, although they failed to find any ACC signal from wide angle X-ray scattering (WAXS). The only direct compositional evidence was obtained with point-by-point TEM-EELS analysis of the carbon edge in incipient nacre tablets[20]. The signal associated with organic molecules was higher in the amorphous than in the crystalline areas, indicating that the amorphous rims contained ACC enriched in organic molecules.

In summary, despite previous research, there is still a high uncertainty about the composition, and, particularly, the distribution of the two phases making up the biocrystals. Accordingly, we have carried out a study on the biogenic calcite of the giant acorn barnacle *Austromegabalanus psittacus* by using high-resolution scanning transmission electron microscopy coupled with EELS (STEM-EELS). In recent studies, EELS has already been used to analyze the chemical composition of biominerals[26,27] because it was able to map the organic and mineral distributions with a spatial resolution better than 1 nm. Here, the use of a STEM

microscope equipped with a latest-generation electron monochromator[28] and a direct-detection camera[29] offers the possibility to detect very weak signals with a spectral resolution down to 7 meV[30], close to those obtained with X-ray based approaches. As demonstrated by Politi et al. from X-ray absorption near-edge structure (XANES) studies[31], the analysis of the calcium L_{23}-edge features provides information on the crystallinity of calcium carbonate phases through the measure of the crystal field splitting (CFS)[32]. In addition to the calcium edge, the carbon K-edge was examined to characterize the distributions of carbonate and organic compounds, which this technique is able to differentiate. Our data reveal that the crystalline phase was found in the form of lumps (mainly composed of calcite), surrounded by amorphous layers made of an organic-rich phase made of ACC+nanocalcite. In this way, we present high-resolution chemical and structural maps of a biocalcite, which, together with results from previous publications, support a different model for biomineralization.

This knowledge is essential in several aspects, but particularly regarding the growth of biominerals. There is hitherto good evidence that calcium carbonate biominerals (by far the most common) form from the crystallization of an amorphous precursor phase (ACC)[33–35]. Nanoroughness has been taken as evidence of growth by a process of attachment of ACC nanoparticles that subsequently crystallize into calcite, by interpreting that the lumps correspond to the initial aggregation particles[18,19,35–37]. This is the so-called crystallization by particle attachment (CPA) hypothesis. It has been recently refuted with the proposal that nanoroughness merely corresponds to the irregular front across which the ACC phase crystallized into crystalline calcium carbonate (CCC)[1,20]. Our structural and compositional data indicate that the separation of the two phases can only be the result of the crystallization process. On this basis, and also taking into account what is presently known from the living biomineralization system, we propose an alternative model for biomineral growth.

RESULTS AND DISCUSSION

Shell morphology

The acorn barnacle *Austromegabalanus psittacus* (Balanidae, Balanomorpha, Cirripedia) has a shell made of six calcitic plates (wall plates) arranged in a cone-like fashion (**Fig. 1a**). It attaches to the substrate by means of a calcareous basal plate. The wall plates grow in width at their contacts. These are mainly delineated by organic membranes, such that the plates can be detached from each other by bleaching (**Fig. 1b, c**). Growth in height takes place at the contact of the wall plates with the basal plate (which only experiences circumferential growth). Sheltering of the soft body within the shell is completed with two pairs of opercular plates (**Fig. 1a**). For further details about the shell structure and morphology of balanids the reader is referred to[38–40].

Topographic analysis by SEM and AFM

SEM observation reveals that the internal (growth) surfaces of the shell plates are studded with calcite grains with diameters from sub-micron to ca. 5 μm in diameter **(Fig. 1d-g**). Grains most commonly display distinct rough surfaces, and, in some cases, flat rhombohedral faces **(Fig. 1f-h**). At first glance, nanoroughness is provided by the development of lumps up to 100-150 nm wide **(Fig. 1h-j**). At higher resolution, the lump surfaces display lower order roughness with smaller lumps up to a few nm **(Fig. 1i-j**). Further observations under the SEM are hampered by lack of resolution.

AFM confirms the nanoroughness and, at the same time, the existence of two phases with different mechanical behaviour in the phase mode **(Fig. 2**). There is a majority phase, which appears in light color in the phase images, and a second dark phase. The height and amplitude images reveal that the dark phase is distributed as a kind of discontinuous 'skin' (pellicles) over the surfaces of the protrusions. Previous measurements on the same material provided pellicle thicknesses of around 1–2 nm[1].

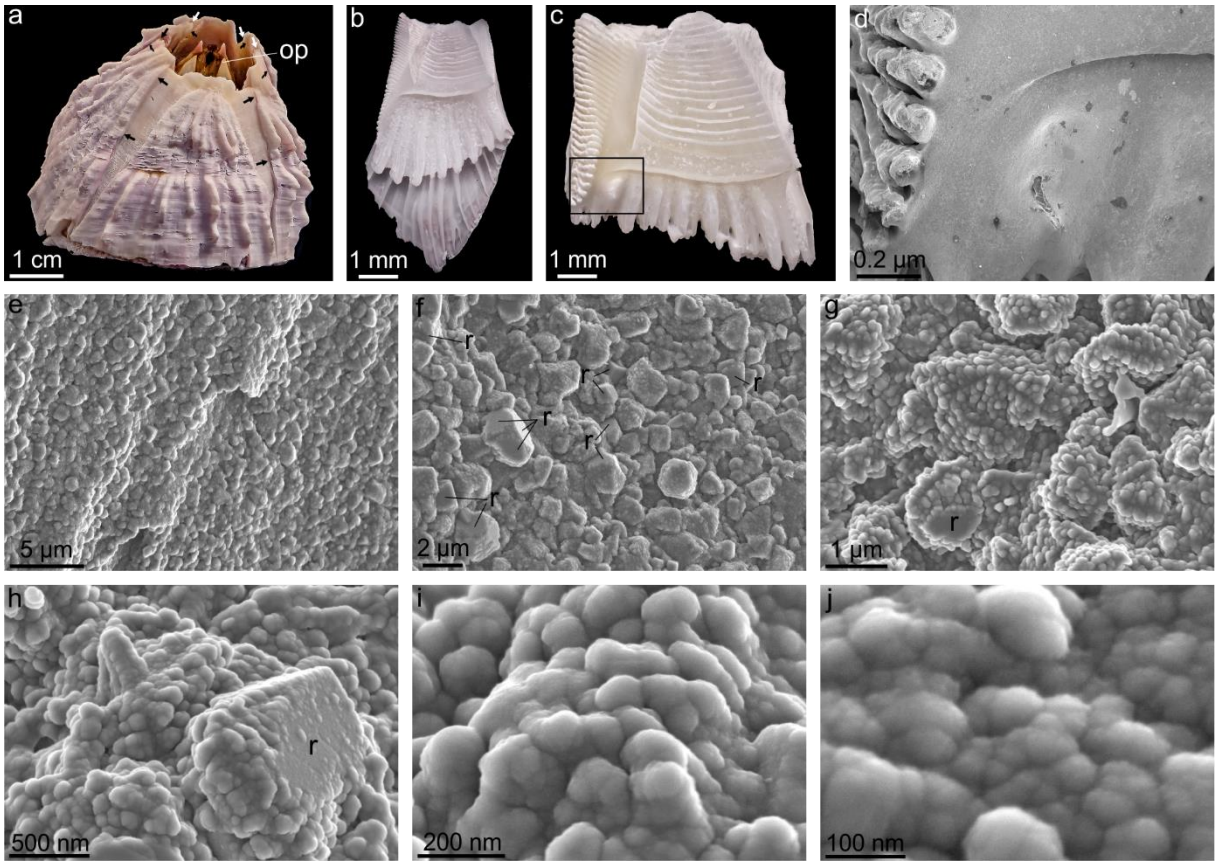

Figure 1. *Shell morphology of* A. psittacus *and observation of the surface nanoroughness of the constituent calcitic grains. (a) Anterior view of a complete specimen; the shell is formed by six plates, whose boundaries are indicated with arrows, and four opercular plates. (b), (c) internal views of two isolated lateral plates. (d) to (j) are progressive SEM close-ups. (d) is a view of the area framed in (c). (e) is a view of the internal surface of a lateral plate, studded with calcite grains. (f) and (g) show the morphology of the grains, from irregular to rhombohedral. (h) to (j) show that nanoroughness consists of protrusions that, in turn, contain smaller protrusions (as small as a few nm), in a fractal-like manner. op= opercular plates, r= smooth rhombohedral faces.*

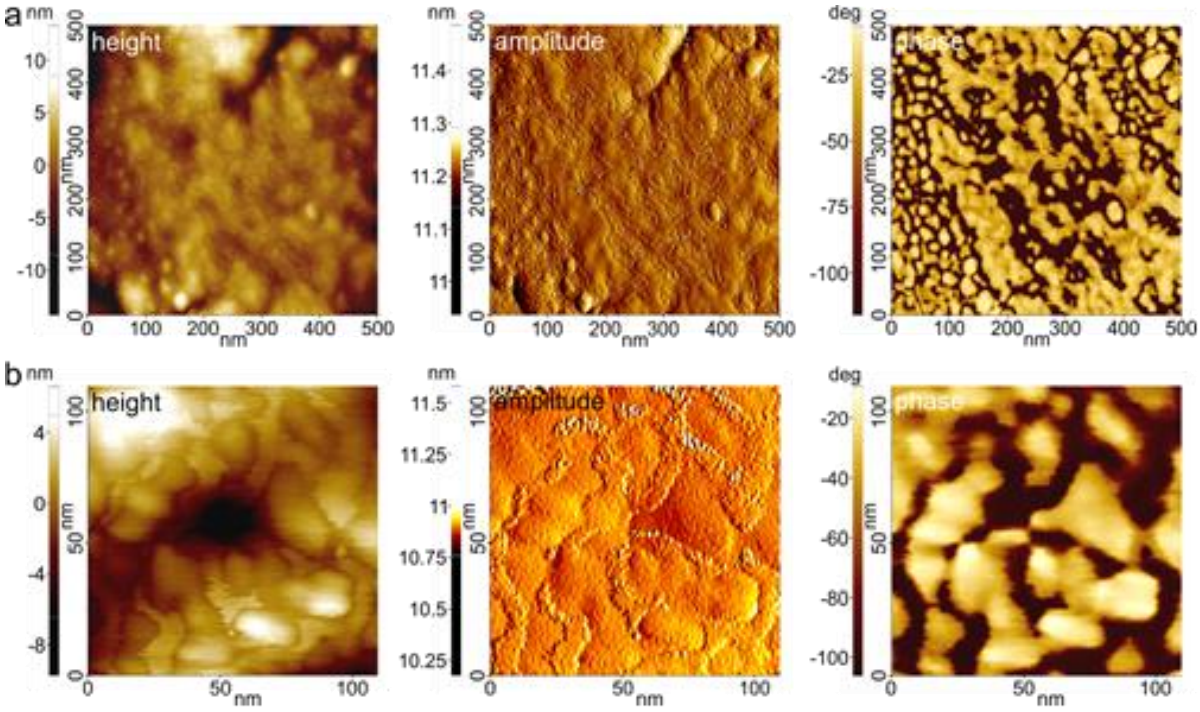

Figure 2. *AFM analysis of the calcitic grains of A. psittacus shell. (a) and (b) are two views of the surfaces of the grains at different magnifications. The nanoroughness, as well as the bi-phase nature of the material, is evident in all cases. The height and amplitude images reveal the distribution of pellicle-like covers of the nanoprotrusions, which appear in a very dark color in the phase image.*

Ultrastructural analysis by TEM

Observation of the mineral particles (micro-fragments) in the TEM (high resolution mode) reveals that the crystal lattice extends over most of the sample, i.e. it is mostly crystalline. In addition, there are non-crystalline areas (lacking visible order and/or a coherent crystal lattice) that are distributed mainly along the edges of the particles, and, more rarely, located within their interiors. These amorphous rims may be up to 20 nm thick. The coexistence of crystalline interiors and amorphous rims is clearly shown in the color orientation maps of **Figure 3**, constructed by selecting the most conspicuous reflections from the fast Fourier transforms (FFTs) of the whole images. Additional evidence for the proposed crystalline and amorphous nature is provided by the FFTs of small areas (~10x10 nm) **(Fig. 3c**, **d**). The presumed amorphous areas within the particle interiors are too small to provide reliable FFTs. We cannot

exclude here that the apparently non-crystalline areas within the particle interior may result from non-selected, almost imperceptible reflections. This is clearly not the case with the amorphous edges. Why the amorphous material concentrates along the edges of the fragments might be due to the amorphous areas being preferential zones of fracture with different composition and mechanical behavior, as indicated by phase mode AFM images. In fact, an elastic vs stiffer behaviour of the dark and light phases respectively was observed[21]. In addition, the edges of particles are particularly thin, such that the amorphous pellicles become easily exposed, whereas toward the interior, where the lamella thickness is much higher (some 50 nm on average), they may easily become masked upon being over-, underlain, or both, by crystalline material.

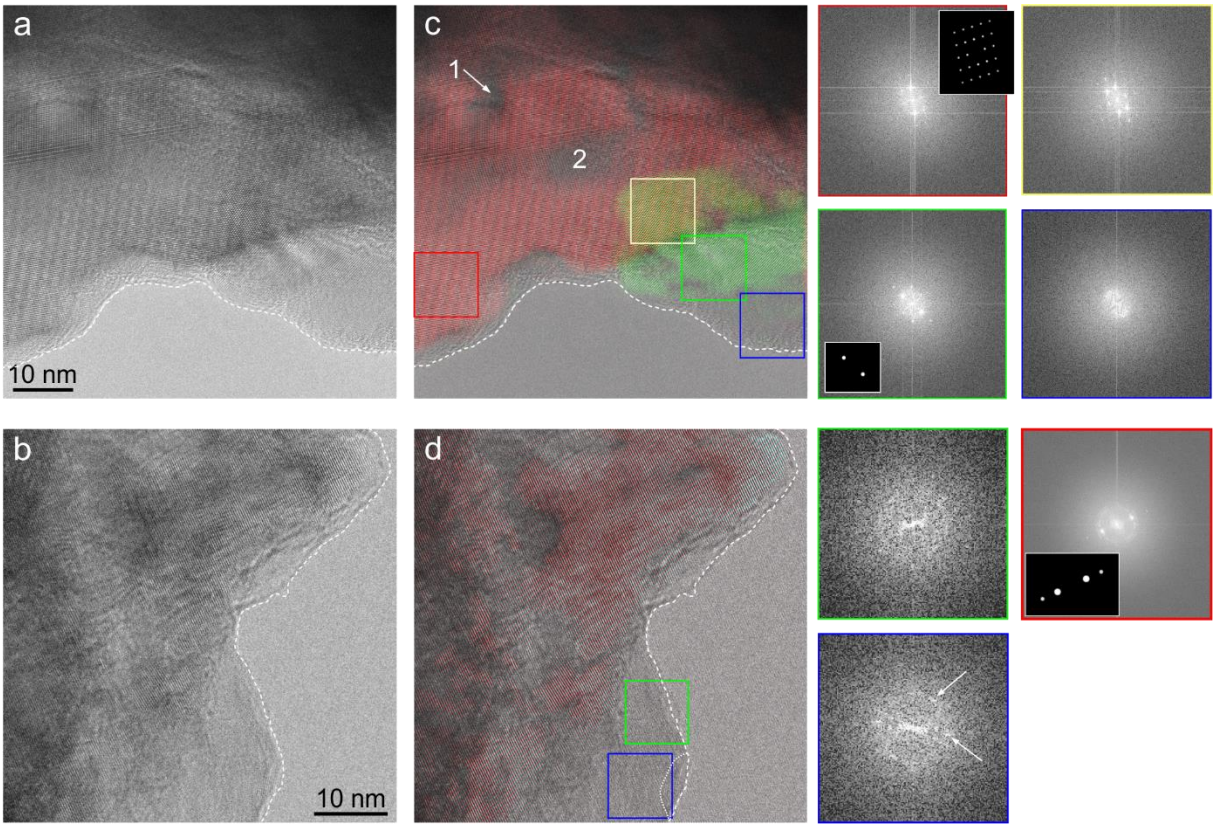

Figure 3. *TEM analysis of the calcite of* A. psittacus *shell. (a), (b) High-resolution TEM views obtained at the edges of particles (the boundaries are indicated with broken lines). The crystal lattice extends over most of the particle, except at the rim and some small internal areas. (c), (d) Color reconstructions of the crystalline areas, obtained by selecting the main reflections. In (c), two different masks have been applied to the local FFTs framed in red and green (small insets within the FFTs framed in red and green), which led to the detection of two main domains*

(red and green), which overlap partly (yellow area). The FFT framed in blue shows that the area is amorphous. The non-colored internal areas might be either amorphous (e.g. position 1) or crystalline, but with reflections that have not been identified (e.g. position 2). In the top dark area, the crystal lattice is not visible due to an excessive thickness of the lamella. In (d), there is a single domain (see general FFT, framed in red, and inserted mask). The reduced FFTs framed in green and blue indicate an amorphous character. Some weak reflections in the lower FFT (arrows) can be attributed to the presence of a domain (indicated tentatively with a dotted line), possibly due to recrystallization by beam damage.

Chemical analysis by high-resolution STEM-EELS

The regions of interest for EELS analysis were localized by STEM-high-angle annular dark field (HAADF) imaging of a focused ion beam (FIB)-produced section of *A. psittacus* shell plate **(Fig. 4a**). As EELS is restricted to thin specimens, around 50 nm, data were recorded on thinner parts corresponding to the darkest regions. The calcite lumps correspond to light areas and boundaries appear as dark contours **(Fig. 4b**). The chemical composition was analysed with a spectral resolution of ~150 meV and electron doses about 10^3 $e^-/Å^2$ (details in **SI**). A complete EEL spectrum was recorded for each pixel position over the scanned area, in the energy range from 280 to 355 eV corresponding to the carbon and calcium edges (K- and L_{23}-edges, respectively) **(Fig. 4c**). The spatial resolution was determined by the pixel size that was fixed at ~ 1-2 nm in order to limit the electron dose and the consequent beam-induced damage. This resolution (far from the ultimate microscope resolution) is one order of magnitude higher than in previous studies on biominerals based on X-ray absorption experiments, where pixel sizes were about 20 nm[41].

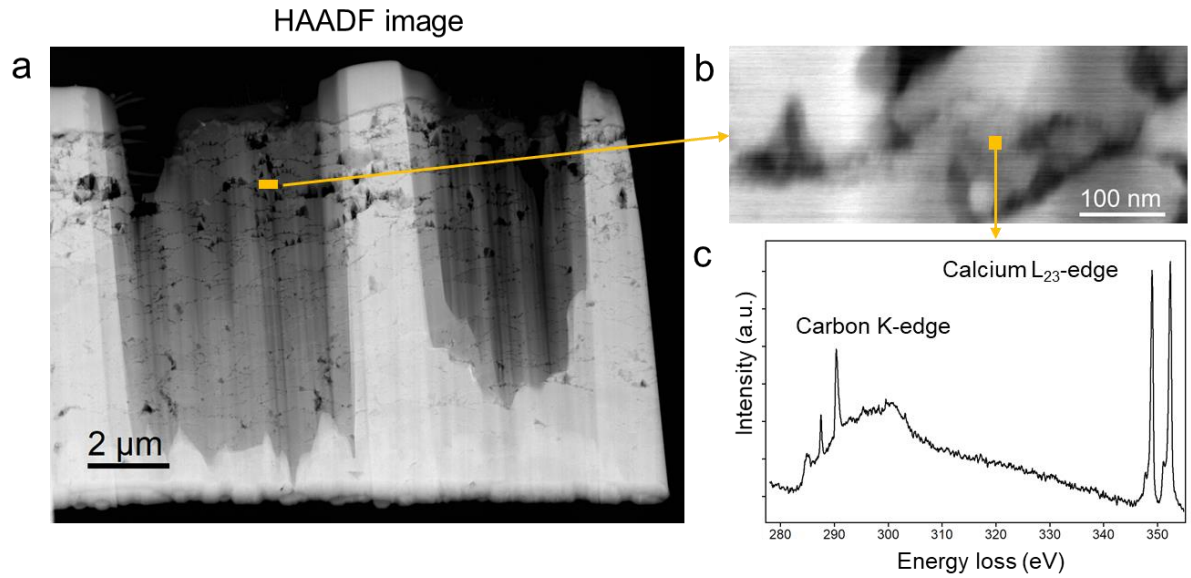

Figure 4*. (a) STEM-HAADF image of the FIB section from a shell plate of* A. psittacus*; (b) Higher magnification of the area indicated by the yellow rectangle in (a); (c) Typical EEL spectrum acquired at the position indicated by the yellow square in (b), showing the carbon K-edge and calcium L_{23}-edge.*

The carbon K-edge was composed of a series of narrow peaks located at energies ranging from ~284eV to ~290eV, corresponding to C 1s → π* electronic transitions, and a broader shoulder characteristic of C 1s → σ* transitions observed around 300 eV. The narrow peak positions vary with the C bonding environment. In the present study, three main peaks were observed. A first one standing at 290.3 eV is attributed to carbonate[42,43] (peak "B" in **Figure 5b**). A second one at 287.4 eV (peak "A" in **Figure 5b**) is attributable to organic carbon bonds according to previous EELS studies on different biominerals and hybrid organic−inorganic composites that have reported a peak located at 286-288 eV associated with the presence of biomolecules[12,26,27,44–46]. A third, broader peak is visible at ~284.5 eV **(Fig. 5b**) corresponding to 1s → π* transitions in C=C bonds that may result from the presence of proteins[47] and/or amorphous carbon originating from partially degraded biomolecules. A combination of these three peaks was observed in variable amounts depending on the position on the shell section. As expected, the carbonate peak is very intense inside the calcite domains and strongly decreases when approaching the boundaries (peak "B" for regions 1 to 4 in **Figure 5a, b**).

Conversely, the organic signal is low inside the calcitic lumps and increases significantly at their edges (peak "A" for regions 1 to 4 in **Figure 5a, b**).

The EELS signature of the Ca L_{23}-edge shows two mains peaks at 349.3 and 352.6 eV (denoted "D" and "F" in **Figure 5c**) resulting from the transitions of a 2p electron to an empty 3d state.

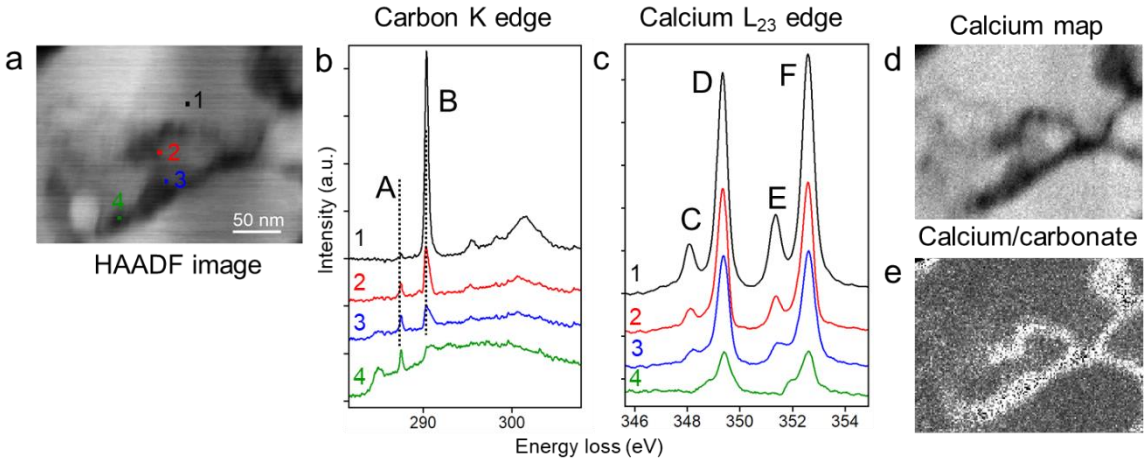

Figure 5. *(a) Enlarged view of the right part of the HAADF image in* ***Figure 4b****; (b) EEL spectra in the energy range corresponding to the carbon K-edge for the different positions indicated by squares in a). Two peaks were detected at about 287.4 eV and 290.3 eV, associated with the presence of organic species (peak A) and carbonate (peak B) respectively; (c) Spectra of the calcium L_{23}-edge for the same positions showing two main peaks at 349.3 eV (peak D) and 352.6 eV (peak F), and two minor ones (peaks C and E). The presented datasets correspond to typical patterns observed in the specimen; (d) Calcium distribution obtained from the integral of the calcium intensity; (e) Ratio between the calcium and the carbonate distributions. The carbonate distribution is deduced from the intensity of peak B on the carbon K-edge (details in* ***SI****).*

The calcium abundancy was mapped by integrating the corresponding edge intensity (details in **SI**, **Figure S2a and S2b**). Calcium maps reveal that the amount of calcium is very low at the lump boundaries **(Fig. 6a**) while the calcium/carbonate ratio reaches its maximum values. Interestingly, this observation indicates that a deficit of carbonate is observed at the boundaries compared to the calcite lump interiors **(Fig. 6b**). The spatial distributions of carbonate and organic species were extracted by performing a gaussian fit of their respective peaks on the

carbon edge (details in **SI**, **Figure S1**). **Figure 6c** presents the distributions of carbonate (in red) and of organic species (in green); other examples can be found in **Figure S3**. The abundancy maps show that a thin layer of organic material of about 10 nm is found surrounding the calcite lumps. Interestingly, the comparison between the distributions of calcium **(Fig. 6a**), the calcium/carbonate ratio **(Fig. 6b**) and the carbonate and organic compounds **(Fig. 6c**) shows that the organic fraction dominates (green areas in **Figure 6c**) in the areas characterized by a lower amount of calcium (compared to calcite interiors) but with a higher calcium/carbonate ratio due to a deficiency in carbonate. In addition, nanometric spots of organics are found in the carbonate areas and conversely, some carbonate nanometric areas are found in the organic parts.

Moreover, EELS data on the Ca-L_{23} edge reveal distinct features at different positions on the specimen (regions 1 to 4 in **Figure 5a, c**). In addition to the major L_{23} lines, minor peaks were detected (denoted "C" and "E" in **Figure 5c**). The calcium L_{23}-edge is known to be highly sensitive to changes in the local atomic arrangement and symmetry. As a consequence, the exact pattern (number, position and intensity of small peaks) is specific to different mineral species. Previous XANES studies have reported significant differences between calcite, aragonite, vaterite, and hydrated and anhydrous amorphous phases of calcium carbonate ($ACC{\cdot}H_2O$ and ACC respectively)[48]. For the present EELS data on *A. psittacus*, CFS values were measured on the L_2 line for each pixel (details in **SI**, **Figure S2**) because, compared to L_3, it provides a higher signal leading to a better precision of the measurements.

CFS measurements have been used in several studies to identify the amorphous calcium carbonate precursors during the formation of mollusk nacre[41] and sea urchin spicules[31,49]. In some studies, calcite was associated with a CFS value of 1.3 eV[48] and in some others with 1.2 eV[49,50]. Here, our CFS values range from 0.8 to 1.3 eV approximately (an example histogram is given in **Figure S2e**) and we choose to establish color (RGB) maps by displaying in green the values below 1.1 eV, in blue from 1.1 to 1.2eV and in red above 1.2 eV **(Fig. 6d**). As

expected, the CFS map **(Fig. 6d)** shows that the CFS reaches its highest values (red areas in **Figure 6d**) inside the calcite domains, which is compatible with our present TEM analysis and with previous observations on biogenic calcites[48,49]. More interestingly, the lowest CFS values (green areas in **Figure 6d**) predominate at the boundaries, which are also characterized by the highest abundancy of the organics **(Fig. 6c)**. Blue spots a few nanometers in size are found within both the red and green areas.

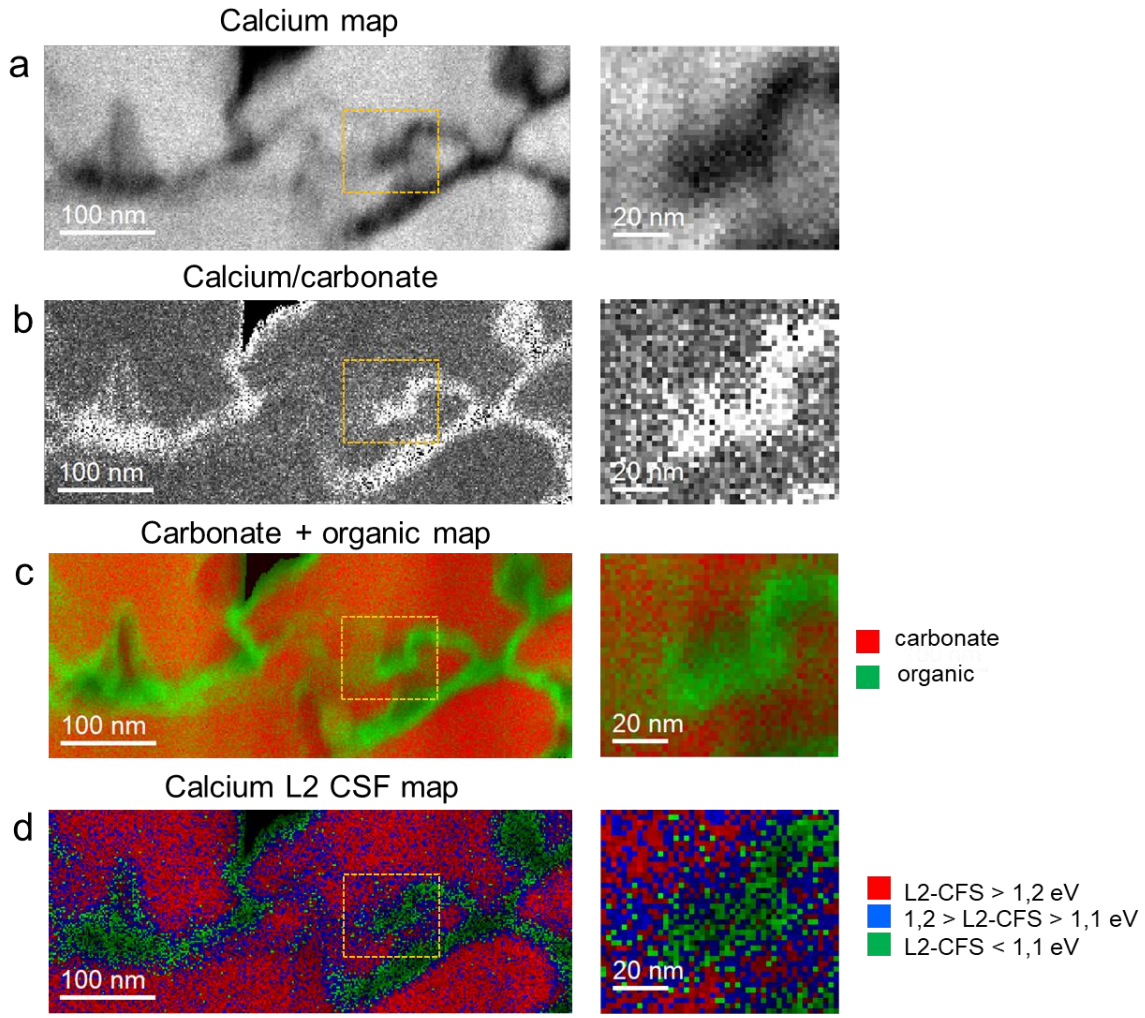

Figure 6. *Maps corresponding to the spatial distributions of: (a) calcium deduced from the integral of the calcium signal from the L_{23} edge; (b) the ratio between calcium and carbonate and (c) color composite map of the spatial distributions of carbonate (in red) and organic compounds (in green). The carbonate and organic abundancies were obtained from their respective signals at 287.4 and 290.3 eV on the carbon K-edge (see details in **SI**, **Figure S1**). (d) Color composite maps of the CFS values (color key provided in the bottom right corner of the image). An enlarged view of the framed area is provided for each map.*

In some studies concerning the formation of biogenic aragonite[41] and calcite[48,49], CFS values equal to 1.1 eV and 1.2 eV were attributed to two different forms of ACC, type 1 and 2. The authors assigned the two forms to ACC·H_2O and anhydrous ACC, respectively. They proposed a model for the formation of aragonite in abalone shell and calcite in sea urchin spicules occurring via the transformation of ACC·H_2O into anhydrous ACC by dehydration, followed by a crystallization step. A recent study using soft X-ray absorption (XAS) calls into question the assignment of type 2 ACC to anhydrous ACC[51] by investigating the phase transformation of ACC when exposed to water vapor (up to 10 mbar) and heat treatment (up to 773 K). These results demonstrate that CFS values are indistinguishable for ACC·H_2O and anhydrous ACC. Moreover, they show that type 2 ACC doesn't correspond to ACC but it is likely to be a "disordered calcium carbonate phase with a nascent calcitic structure with a short range order at the nanometer scale" denoted hereafter as "nano-calcite". These authors suggest a revised the formation pathway of the biogenic calcite as ACC·H_2O → disordered nano-calcite → calcite.

Concerning the CFS values, Tsao et al.[51] measured 1.11 eV for nano-calcite (commercial calcite), 1.23 eV for micro-calcite (synthetic calcite) and below 1.1 eV for ACC, with no distinction between the hydrated and anhydrous forms. Following these authors, the green areas in **Fig. 6d** (CFS < 1.1 eV) can be attributed to ACC and the blue and red ones (CFS > 1.1 eV) to nano- or micro-calcite. So, we present all values above 1.1 eV (blue and red in **Fig. 6d**) with the same color (purple in **Fig. 7**) corresponding to a crystalline phase. We cannot determine whether the purple spots visible in green amorphous areas (**Fig. 7**) correspond to nanocrystals lying above, below or within the amorphous calcium carbonate.

Finally, the comparison between organic (**Fig. 7a and b**) and structural phase (**Fig. 7c and d**) maps indicates that organics are mainly found in the ACC areas, although small spots are also present in the calcitic lumps. Due to their nanometric sizes, all spots (ACC spots in

crystal lumps and organic spots in calcitic domains) are visible in our experiments thanks to the STEM-EELS high spatial resolution (1-2 nm) but they cannot be detected with X-ray resolutions (~ 20 nm at its best).

As commented in the introduction, the only reliable data were obtained with the help of TEM. High resolution imaging led to the observation of amorphous areas both around nacre tablets (aragonite)[25] and within the sea urchin spine (calcite)[12]. Both studies reached the conclusion that the amorphous material contained ACC, either by recrystallizing it into aragonite[25], or by differential etching[12]. Substantial evidence obtained with TEM-EELS in growing gastropod nacre tablets[20] showed that the signal of organic molecules increased from the crystalline to the amorphous areas, thus indicating that the latter contained ACC relatively enriched in biomolecules. Our extremely high-resolution maps show the exact distribution of the calcite interiors and their ACC+nanocalcite+organic cortexes. These appear discontinuous, thus allowing continuity of the crystal lattice. This evidence constitutes a significant step toward the knowledge of the intimate structure of biominerals.

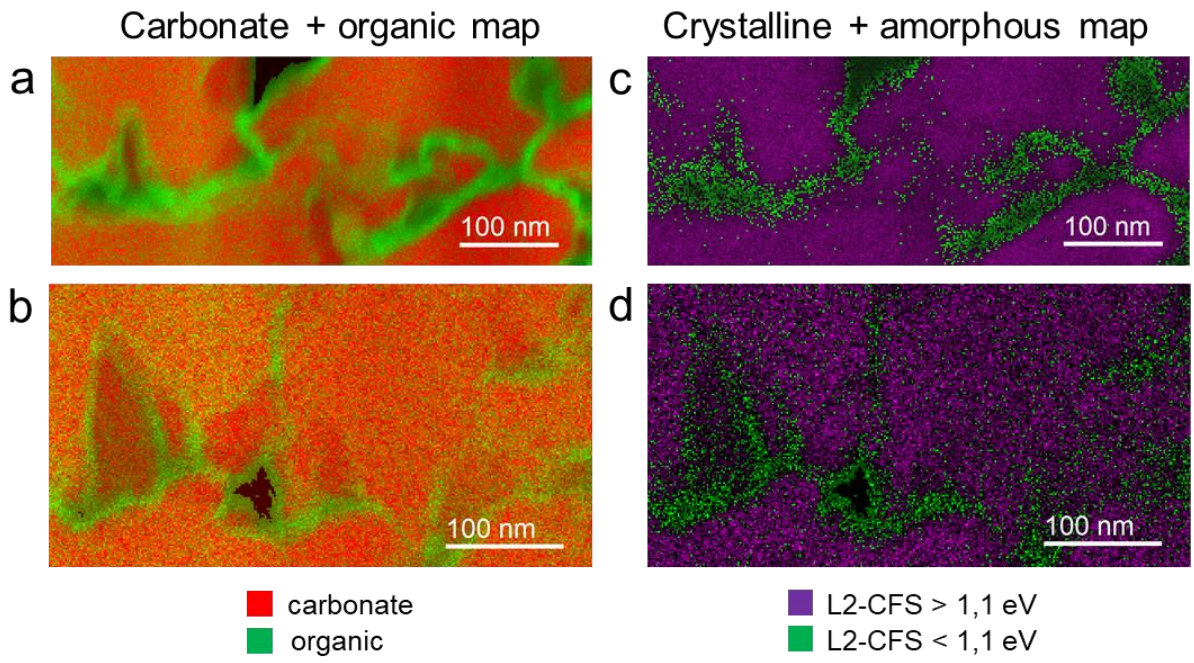

Figure 7. *Comparison for two different areas: in (a) and (b) the distributions of carbonate (in red) and organic compounds (in green) are shown. (c) and (d) are maps of the crystalline vs amorphous nature of the mineral phase. The amorphous areas (CFS values < 1.1 eV) are represented in green and crystalline ones (CFS values > 1.1 eV) in purple.*

Model for the formation of the calcite biominerals

AFM, TEM and STEM-EELS data indicate that the calcite forming the *A. psittacus* shell does not have a homogeneous composition, but is made of two different phases, a crystalline, calcitic phase, and an amorphous phase made from a mixture of calcium, carbonate and organics (referred to hereafter as "ACC-like phase"). The crystalline phase is distributed in the form of lumps, surrounded by cortexes made of the ACC-like phase. The presence of organics with a strong calcium binding capacity could explain the accumulation of calcium not bound to carbonate in the carbonate-deficient regions. The different methods provide different thicknesses for the cortexes, being much thinner when measured with AFM. One of the reasons might be that the AFM is a 3D surface observation, whereas both TEM and STEM-EELS observations record properties across the thickness of a slice of the material. The double phase (bi-phase) nanostructure observed is highly relevant regarding the mode of biocrystal growth. There is hitherto consensus in that calcium carbonate biominerals form from an ACC phase containing organic molecules, e.g.[12,19,33,34,37]. Within this precursor phase (dense liquid phase of ACC plus organics[33,52]), the distribution of components would be homogeneous[33,53] and the demixing and segregation of organics to the lump surfaces occurs during crystallization of most of the ACC into calcite. This mechanism was proposed for the formation of amorphous rims around crystalline nano-units, in the sea urchin spicule[12]. According to this model, crystallization of ACC into calcite led to both biomacromolecule expelling from and occlusion within the newly formed crystal lattice. Growth of the calcite nanocrystal was terminated when a critical biomolecule concentration was reached in the growth layer, which inhibited further crystallization and resulted in the formation of an ACC layer on the nanoparticle surface. A

similar mechanism was invoked for the sea urchin spines and test plates[54], gastropod nacre[20], and the calcite of cirripeds.[1]

A couple of years later, Gal. et al.[37] proposed that the lumps producing the surface nanoroughness represent the original amorphous aggregation units. This hypothesis is known as the crystallization by particle attachment (CPA) hypothesis[18,19,35–37], and has become prevalent today. This hypothesis encounters two difficulties. First, lumps in biominerals have a large range of sizes, from a few nm to ~200 nm. Large sizes are difficult to reconcile with the exceedingly small dimensions of the extrapallial space observed in bivalves (90-100 nm in thickness)[55,56] and brachiopods (<50 nm)[13] and with the small diameters of the pores in gastropod nacre interlamellar membranes, through which they have to percolate[57]. Second, it has been revealed that the lumps elongate and/or align in parallel to the strongest periodic bond chains (PBCs) in both aragonite (a-axis)[20] and in calcite (-441 directions)[1]. Additional details and examples of both cases are provided in **SI**, **Figure S4**. That is, they are crystallographic features, formed upon the conversion of ACC into calcite. Taking all this into account, we develop a model which is also consistent with the composition at the nanoscale observed in the present study. **Figure 8** depicts the process for the production of biocalcite. The precursor phase is produced by the aggregation of nanoparticles (ACC phase + organic molecules), perhaps together with ions (as implied also by Gal et al.[37]), and forms a rim around the crystal **(Fig. 8a**). Although there are no indications about the size of aggregation nanoparticles, they should be much smaller than the extrapallial spaces, perhaps on the order of a few tens of nanometers. The crystallization front takes a complex shape, thus producing the typical nanoroughness, i.e. the nanoroughness originates during the transformation of ACC into crystalline. Similar nanoroughness with fractal behavior/ cauliflower-like surfaces has been described in thin films formed by atomic deposition with the main mechanism for the nanoroughness being self-

shadowing. This occurs in low mobility conditions in which atoms stick to the first site at which they arrive, creating protuberances that capture more atoms and shadow surrounding areas[58].

Demixing happens because organic molecules cannot be incorporated into the crystal lattice along those crystallographic directions that constitute periodic bond chains (PBCs), along which ionic bonds are particularly strong **(Fig. 8b**). As a consequence, during crystallization, the organic molecules become expelled sideward from those directions, thus forming the cortexes **(Fig. 8c**), where they coexist with some residual, permanently stabilized ACC. This expulsion of the organic material from the crystal lattice resembles a purification process by crystallization. A good analogy to directional expelling along the PBC is soil displacement during groove plowing for field cultivation, although this happens in a much more ordered way. The high calcium to carbonate ratio measured in the organic-rich cortexes can be explained if part of the calcium is bound to biomolecules. Then it would have to migrate with its binding molecules to the cortexes. Crystallization by dissolution-reprecipitation could facilitate the movements of organics across distances of tens of nm, which is easier to envisage than the diffusion of the biomolecules through a solid mineral phase[59,60].

Our model invokes the demixing-by-crystallization process of Seto et al.[12] although it is quite different from the rest of their model. Unlike us, these authors established the following stages: (1) nucleation initiates, simultaneously or sequentially, at different sites, (2) growth of the calcite nanocrystal terminates when a critical macromolecule concentration is reached at the growth edges, and (3) particles aggregate, possibly by oriented attachment, and the lattice extends across particles through mineral bridges. Our model is consistent with the CPA model provided that the notion of nanoprotrusions being the original attachment particles is removed. It has the additional advantages of being consistent with (1) the substantial direct evidence we provide on the internal composition of the biomineral, (2) the nature of protrusions as crystallographically-controlled features, and (3) the known dimensions of the extrapallial

spaces. To sum up, (1) and (2) can only be explained by crystallization of calcite from an amorphous precursor, whereas (2) and (3) preclude the possibility that the nanoprotrusions are the “frozen” (crystallized) original attachment amorphous nanoparticles.

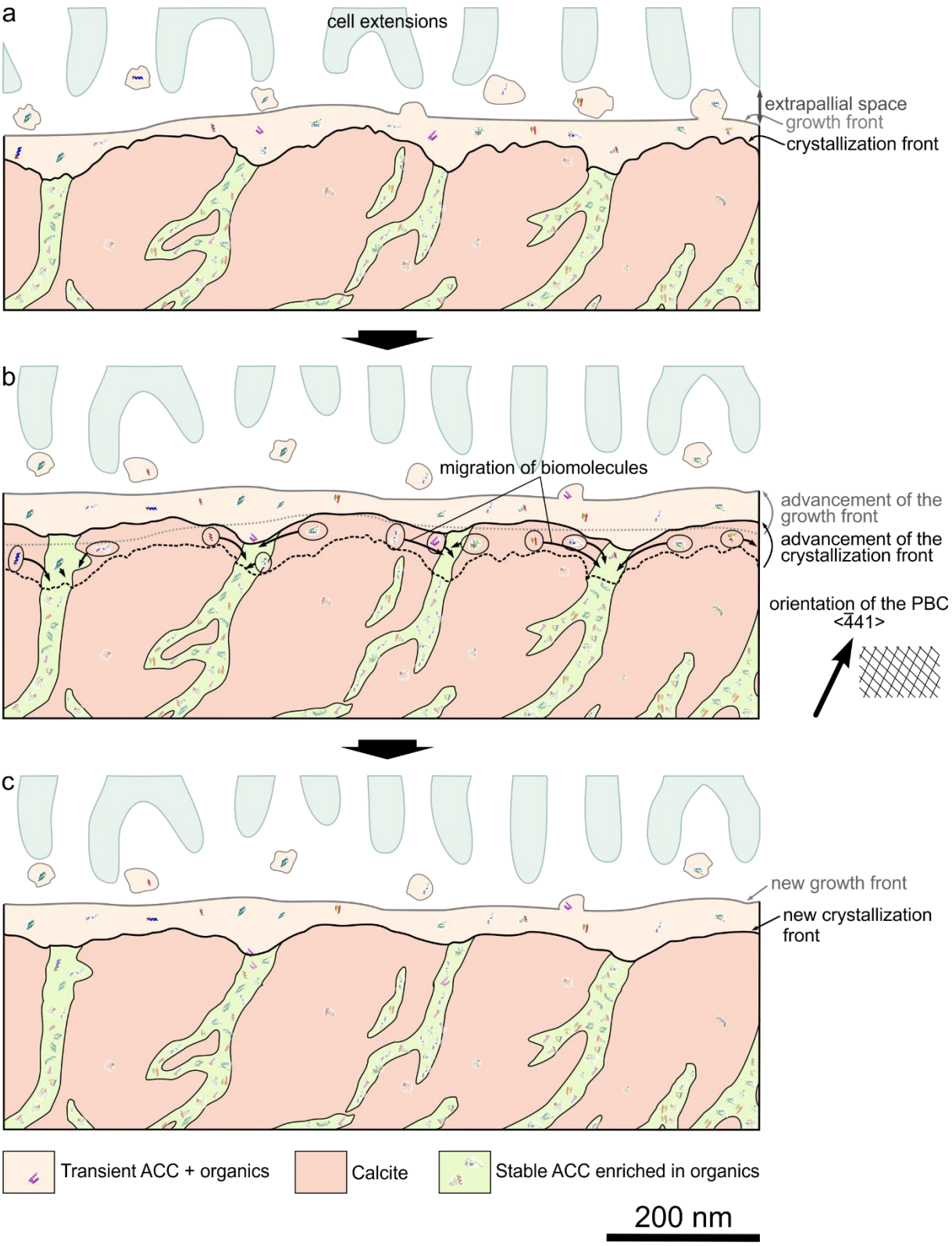

Figure 8*. Model for the formation of the bi-phase nanostructure of calcite biominerals. (a). The mantle cells deliver ACC+biomolecules nanoparticles small enough the be accommodated within the reduced extrapallial space, between the mantle cells and the surface of the forming crystal. The dimensions of this space are hypothetical, based on the information available mainly from molluscs. At the surface of the crystals, the nanoparticles feed a (presumably permanent) cortex of ACC with biomolecules, below which the ACC crystallizes into calcite across an irregular crystallization front. (b). With time, both the growth and the crystallization*

fronts migrate. Upon crystallization, the biomolecules cannot easily be incorporated along the PBCs (particularly the <-441> PBC of calcite) and are expelled sideward. As a result, they become concentrated in particular pellicle-like regions, where they stabilize some residual ACC. In this way, the calcitic cores of the nanoprotrusions roughly elongate in the direction of the PBC. (c). The final outcome is the production of a biocrystal characterized by a bi-phase composition.

CONCLUSIONS

We present compositional and structural maps of a biomineral at nanometric resolution. Our maps clearly show the existence of two compositional phases: (1) a crystalline (calcite) phase and (2) an amorphous phase composed of biomolecules and ACC. The first phase forms lumps surrounded by discontinuous cortexes of the amorphous phase. In this way, the crystal lattice extends across the biocrystal. The reported structure is only compatible with a process of demixing of the organic molecules from the initial phase during the process of crystallization. In this way, we do not only provide critical evidence for the structure of biominerals, but also for their mode of growth. Future additional evidence (e.g. improvement of the compositional data, detection of the organic-rich ACC precursor phase) will help in refining or modify the proposed growth model.

EXPERIMENTAL SECTION

Sample preparation

Specimens of the giant barnacle *Austromegabalanus psittacus* (order Balanomorpha, family Balanidae) were sampled alive in Isla Santa María, some 30 km NW of Antofagasta (ca. 23.4°S, northern Chile). The specimens were freeze-dried at the Centro de Investigación e Innovación para el Cambio Climático (Universidad Santo Tomás, Santiago de Chile) before being shipped to the University of Granada (Spain).

Scanning electron microscopy (SEM)

Organic remains were removed from the surfaces of the barnacle plates by immersion in commercial bleach (~ 5% active chlorine) for 4-5 min. They were later ultrasonicated and dried in an oven at 60°. Carbon-coating (Emitech K975X carbon evaporator) preceded observations with the field emission SEMs (FESEMs) Zeiss Auriga and FEI QemScan 650F atthe Centre for Scientific Instrumentation (CIC) of the University of Granada (UGR). Some samples were observed with the Ultra high-resolution FESEMs ThermoFisher Scientific Apreo and Verios G4, housed at NanoPort Europe (Eindhoven, The Netherlands).

Focused Ion Beam (FIB) milling

FIB milling was performed on the internal surface of a lateral plate using a Hitachi NX5000 Ethos FIB/SEM, operated at 30 kV. Milling was made at 12 nA and 30 kV, followed by fine polishing at 1.5 nA and 10kV. A thin section measuring approximatively 100 nm in thickness was prepared. Nevertheless, the contacts between grains were etched preferentially, which resulted in the frequent formation of holes at these positions **(Fig. 4a**).

Transmission electron microscopy (TEM)

Fragments were obtained from a lateral plate by scraping its surface with a wooden tool. These were then gently ground in an agate mortar. The powder was then suspended in pure ethanol, and the solution was dropped onto lacy carbon copper grids and air-dried. TEM observations and measurements were done using a double Cs corrected JEOL JEM-ARM200F TEM (Max Planck Institute of Colloids and Interfaces, Potsdam) equipped with a cold-field emission gun and a Gatan OneView camera. The machine was operated in TEM mode at 200 kV, 5 μA emission current and 500 μs exposure time using low dose technique. Crystallographic domains were indexed by Fast Fourier Transform (FFT) analysis.

Atomic force microscopy (AFM)

Observations were done on the growth surfaces of plates and primary septa. We used a Park Systems NX20 microscope equipped with a MikroMasch NSC14 (K = 5 N/m, F = 160 kHz) cantilever (CIC, UGR). We worked in tapping mode and recorded height, amplitude and phase signals. Images were analysed with Park Systems XEI 4.3 software.

Scanning transmission electron microscopy-electron energy loss spectroscopy (STEM-EELS)

HAADF images and EELS data were acquired using a Cs-corrected Nion Hermes 200-S microscope operated at 100 kV, equipped with a gun monochromator, a Nion Iris spectrometer and a single tilt cryo-specimen holder (LN_2 cooling holder from Henny Z), to minimize beam radiation damage, and a Merlin Direct Electron Detector camera (Quantum Detectors, UK), used for spectroscopic analysis. The monochromated electron beam provides ultra-high energy resolutions for spectroscopic analysis down to 7 meV[30]. EELS data were acquired in the spectrum-imaging mode[61] in which the electron beam is scanned over the area

of interest and a whole spectrum is acquired at each position. A typical hyperspectral image contains about 10000 spectra.

SUPPORTING INFORMATION

The Supporting Information is available free of charge at https://pubs.acs.org/doi/10.1021/acsnano.XXX.

Additional details concerning the acquisition conditions, processing and analysis of EELS data; NLLS fitting of the carbon K-edge; Crystal field splitting (CFS) measurements and associated maps; Additional carbonate and organics maps in different areas; Detailed morphology of nanoprotrusions (PDF).

ACKNOWLEDGMENTS

Elena Macías-Sánchez (UGR) carried out the TEM analysis. Nelson A. Lagos (Univ. Santo Tomás, Santiago de Chile) procured specimens of *Austromegabalanus psittacus*. We thank Juliette Gambado (Université de Paris-Saclay) for preliminary experiments and Mike Walls (LPS, CNRS Université de Paris-Saclay) for his proofreading and corrections of the manuscript. This research was funded by projects PID2020-116660GB-I00 of the Spanish Ministerio de Ciencia e Innovación, B-RNM-265-UGR18 and P20-00207 of the Junta de Andalucía, the Unidad Científica de Excelencia UCE-PP2016-05 of the University of Granada (AGC, ABRN), and the Research Group RNM363 of the Junta de Andalucía (AGC). This work has been partly supported by the National Agency for Research under the Program of Future Investment TEMPOS CHROMATEM (Reference no. ANR-10-EQPX-50) and the European Union's Horizon 2020 Research and Innovation Program (Grant no. 823717, ESTEEM3).

REFERENCES

(1) Checa, A. G.; Macías-Sánchez, E.; Rodríguez-Navarro, A. B.; Sánchez-Navas, A.; Lagos, N. A. Origin of the Biphase Nature and Surface Roughness of Biogenic Calcite Secreted by the Giant Barnacle *Austromegabalanus Psittacus*. *Sci Rep* **2020**, *10* (1), 16784. https://doi.org/10.1038/s41598-020-73804-8.

(2) Mutvei, H. Ultrastructure of the Mineral and Organic Components of Molluscan Nacreous Layers. *Biomineralization* **1970**, *2*, 49–72.

(3) Mutvei, H. On the Internal Structure of the Nacreous Tablets in Molluscan Shells. *Scanning Electron Microsc.* **1979**, *2*, 457–462.

(4) Dauphin, Y. Nanostructures de la Nacre des Tests de Céphalopodes Actuels. *Paläontol Z* **2001**, *75* (1), 113–122. https://doi.org/10.1007/BF03022601.

(5) Dauphin, Y. Structure and Composition of the Septal Nacreous Layer of *Nautilus Macromphalus* L. (Mollusca, Cephalopoda). *Zoology (Jena)* **2006**, *109* (2), 85–95. https://doi.org/10.1016/j.zool.2005.08.005.

(6) Dauphin, Y. The Nanostructural Unity of Mollusc Shells. *Mineralogical Magazine* **2008**, *72* (1), 243–246. https://doi.org/10.1180/minmag.2008.072.1.243.

(7) Bruet, B. J. F.; Qi, H. J.; Boyce, M. C.; Panas, R.; Tai, K.; Frick, L.; Ortiz, C. Nanoscale Morphology and Indentation of Individual Nacre Tablets from the Gastropod Mollusc *Trochus Niloticus*. *Journal of Materials Research* **2005**, *20* (9), 2400–2419. https://doi.org/10.1557/jmr.2005.0273.

(8) Rousseau, M.; Lopez, E.; Stempflé, P.; Brendlé, M.; Franke, L.; Guette, A.; Naslain, R.; Bourrat, X. Multiscale Structure of Sheet Nacre. *Biomaterials* **2005**, *26* (31), 6254–6262. https://doi.org/10.1016/j.biomaterials.2005.03.028.

(9) Li, X.; Chang, W.-C.; Chao, Y. J.; Wang, R.; Chang, M. Nanoscale Structural and Mechanical Characterization of a Natural Nanocomposite Material: The Shell of Red Abalone. *Nano Lett.* **2004**, *4* (4), 613–617. https://doi.org/10.1021/nl049962k.

(10) Sethmann, I.; Hinrichs, R.; Wörheide, G.; Putnis, A. Nano-Cluster Composite Structure of Calcitic Sponge Spicules--a Case Study of Basic Characteristics of Biominerals. *J Inorg Biochem* **2006**, *100* (1), 88–96. https://doi.org/10.1016/j.jinorgbio.2005.10.005.

(11) Przeniosło, R.; Stolarski, J.; Mazur, M.; Brunelli, M. Hierarchically Structured Scleractinian Coral Biocrystals. *J Struct Biol* **2008**, *161* (1), 74–82. https://doi.org/10.1016/j.jsb.2007.09.020.

(12) Seto, J.; Ma, Y.; Davis, S. A.; Meldrum, F.; Gourrier, A.; Kim, Y.-Y.; Schilde, U.; Sztucki, M.; Burghammer, M.; Maltsev, S.; Jäger, C.; Cölfen, H. Structure-Property Relationships of a Biological Mesocrystal in the Adult Sea Urchin Spine. *Proc Natl Acad Sci U S A* **2012**, *109* (10), 3699–3704. https://doi.org/10.1073/pnas.1109243109.

(13) Simonet Roda, M.; Griesshaber, E.; Ziegler, A.; Rupp, U.; Yin, X.; Henkel, D.; Häussermann, V.; Laudien, J.; Brand, U.; Eisenhauer, A.; Checa, A. G.; Schmahl, W. W. Calcite Fibre Formation in Modern Brachiopod Shells. *Sci Rep* **2019**, *9*, 598. https://doi.org/10.1038/s41598-018-36959-z.

(14) Dauphin, Y.; Dufour, E. Nanostructures of the Aragonitic Otolith of Cod (*Gadus Morhua*). *Micron* **2008**, *39* (7), 891–896. https://doi.org/10.1016/j.micron.2007.11.007.

(15) Pérez-Huerta, A.; Dauphin, Y. Comparison of the Structure, Crystallography and Composition of Eggshells of the Guinea Fowl and Graylag Goose. *Zoology (Jena)* **2016**, *119* (1), 52–63. https://doi.org/10.1016/j.zool.2015.11.002.

(16) Henriksen, K.; Stipp, S. L. S.; Young, J. R.; Bown, P. R. Tailoring Calcite: Nanoscale AFM of Coccolith Biocrystals. *American Mineralogist* **2003**, *88* (11–12), 2040–2044. https://doi.org/10.2138/am-2003-11-1248.

(17) Henriksen, K.; Young, J. R.; Bown, P. R.; Stipp, S. L. S. Coccolith Biomineralisation Studied with Atomic Force Microscopy. *Palaeontology* **2004**, *47* (3), 725–743. https://doi.org/10.1111/j.0031-0239.2004.00385.x.

(18) Wolf, S. E.; Böhm, C. F.; Harris, J.; Demmert, B.; Jacob, D. E.; Mondeshki, M.; Ruiz-Agudo, E.; Rodríguez-Navarro, C. Nonclassical Crystallization in Vivo et in Vitro (I): Process-Structure-

Property Relationships of Nanogranular Biominerals. *J Struct Biol* **2016**, *196* (2), 244–259. https://doi.org/10.1016/j.jsb.2016.07.016.

(19) Rodríguez-Navarro, C.; Ruiz-Agudo, E.; Harris, J.; Wolf, S. E. Nonclassical Crystallization *in Vivo* et *in Vitro* (II): Nanogranular Features in Biomimetic Minerals Disclose a General Colloid-Mediated Crystal Growth Mechanism. *J Struct Biol* **2016**, *196* (2), 260–287. https://doi.org/10.1016/j.jsb.2016.09.005.

(20) Macías-Sánchez, E.; Willinger, M. G.; Pina, C. M.; Checa, A. G. Transformation of ACC into Aragonite and the Origin of the Nanogranular Structure of Nacre. *Sci Rep* **2017**, *7* (1), 12728. https://doi.org/10.1038/s41598-017-12673-0.

(21) Li, X.; Xu, Z.-H.; Wang, R. In Situ Observation of Nanograin Rotation and Deformation in Nacre. *Nano Lett.* **2006**, *6* (10), 2301–2304. https://doi.org/10.1021/nl061775u.

(22) Nouet, J.; Baronnet, A.; Howard, L. Crystallization in Organo-Mineral Micro-Domains in the Crossed-Lamellar Layer of Nerita Undata (Gastropoda, Neritopsina). *Micron* **2012**, *43* (2), 456–462. https://doi.org/10.1016/j.micron.2011.10.027.

(23) Baronnet, A.; Cuif, J. P.; Dauphin, Y.; Farre, B.; Nouet, J. Crystallization of Biogenic Ca-Carbonate within Organo-Mineral Micro-Domains. Structure of the Calcite Prisms of the Pelecypod *Pinctada Margaritifera* (Mollusca) at the Submicron to Nanometre Ranges. *Mineralogical Magazine* **2008**, *72* (2), 617–626. https://doi.org/10.1180/minmag.2008.072.2.617.

(24) Checa, A. G.; Mutvei, H.; Osuna-Mascaró, A. J.; Bonarski, J. T.; Faryna, M.; Berent, K.; Pina, C. M.; Rousseau, M.; Macías-Sánchez, E. Crystallographic Control on the Substructure of Nacre Tablets. *J Struct Biol* **2013**, *183* (3), 368–376. https://doi.org/10.1016/j.jsb.2013.07.014.

(25) Nassif, N.; Pinna, N.; Gehrke, N.; Antonietti, M.; Jäger, C.; Cölfen, H. Amorphous Layer around Aragonite Platelets in Nacre. *Proc Natl Acad Sci U S A* **2005**, *102* (36), 12653–12655. https://doi.org/10.1073/pnas.0502577102.

(26) Ajili, W.; Tovani, C. B.; Fouassier, J.; de Frutos, M.; Laurent, G. P.; Bertani, P.; Djediat, C.; Marin, F.; Auzoux-Bordenave, S.; Azaïs, T.; Nassif, N. Inorganic Phosphate in Growing Calcium Carbonate Abalone Shell Suggests a Shared Mineral Ancestral Precursor. *Nat Commun* **2022**, *13* (1), 1496. https://doi.org/10.1038/s41467-022-29169-9.

(27) Gay, C.; Letavernier, E.; Verpont, M.-C.; Walls, M.; Bazin, D.; Daudon, M.; Nassif, N.; Stéphan, O.; de Frutos, M. Nanoscale Analysis of Randall's Plaques by Electron Energy Loss Spectromicroscopy: Insight in Early Biomineral Formation in Human Kidney. *ACS Nano* **2020**, *14* (2), 1823–1836. https://doi.org/10.1021/acsnano.9b07664.

(28) Colliex, C. From Early to Present and Future Achievements of EELS in the TEM. *Eur. Phys. J. Appl. Phys.* **2022**, *97*, 38. https://doi.org/10.1051/epjap/2022220012.

(29) Hart, J. L.; Lang, A. C.; Leff, A. C.; Longo, P.; Trevor, C.; Twesten, R. D.; Taheri, M. L. Direct Detection Electron Energy-Loss Spectroscopy: A Method to Push the Limits of Resolution and Sensitivity. *Sci Rep* **2017**, *7* (1), 8243. https://doi.org/10.1038/s41598-017-07709-4.

(30) Li, X.; Haberfehlner, G.; Hohenester, U.; Stéphan, O.; Kothleitner, G.; Kociak, M. Three-Dimensional Vectorial Imaging of Surface Phonon Polaritons. *Science* **2021**, *371* (6536), 1364–1367. https://doi.org/10.1126/science.abg0330.

(31) Politi, Y.; Metzler, R. A.; Abrecht, M.; Gilbert, B.; Wilt, F. H.; Sagi, I.; Addadi, L.; Weiner, S.; Gilbert, P. U. P. A. Transformation Mechanism of Amorphous Calcium Carbonate into Calcite in the Sea Urchin Larval Spicule. *Proc Natl Acad Sci U S A* **2008**, *105* (45), 17362–17366. https://doi.org/10.1073/pnas.0806604105.

(32) Rez, P.; Blackwell, A. Ca L23 Spectrum in Amorphous and Crystalline Phases of Calcium Carbonate. *J. Phys. Chem. B* **2011**, *115* (38), 11193–11198. https://doi.org/10.1021/jp203057y.

(33) Gower, L. B. Biomimetic Model Systems for Investigating the Amorphous Precursor Pathway and Its Role in Biomineralization. *Chem Rev* **2008**, *108* (11), 4551–4627. https://doi.org/10.1021/cr800443h.

(34) Weiner, S.; Mahamid, J.; Politi, Y.; Ma, Y.; Addadi, L. Overview of the Amorphous Precursor Phase Strategy in Biomineralization. *Front. Mater. Sci. China* **2009**, *3* (2), 104–108. https://doi.org/10.1007/s11706-009-0036-x.

(35) Gilbert, P. U. P. A.; Bergmann, K. D.; Boekelheide, N.; Tambutté, S.; Mass, T.; Marin, F.; Adkins, J. F.; Erez, J.; Gilbert, B.; Knutson, V.; Cantine, M.; Hernández, J. O.; Knoll, A. H. Biomineralization: Integrating Mechanism and Evolutionary History. *Science Advances* **2022**, *8* (10), eabl9653. https://doi.org/10.1126/sciadv.abl9653.

(36) De Yoreo, J. J.; Gilbert, P. U. P. A.; Sommerdijk, N. A. J. M.; Penn, R. L.; Whitelam, S.; Joester, D.; Zhang, H.; Rimer, J. D.; Navrotsky, A.; Banfield, J. F.; Wallace, A. F.; Michel, F. M.; Meldrum, F. C.; Cölfen, H.; Dove, P. M. Crystallization by Particle Attachment in Synthetic, Biogenic, and Geologic Environments. *Science* **2015**, *349* (6247), aaa6760. https://doi.org/10.1126/science.aaa6760.

(37) Gal, A.; Kahil, K.; Vidavsky, N.; DeVol, R. T.; Gilbert, P. U. P. A.; Fratzl, P.; Weiner, S.; Addadi, L. Particle Accretion Mechanism Underlies Biological Crystal Growth from an Amorphous Precursor Phase. *Advanced Functional Materials* **2014**, *24* (34), 5420–5426. https://doi.org/10.1002/adfm.201400676.

(38) Checa, A. G.; Salas, C.; Rodríguez-Navarro, A. B.; Grenier, C.; Lagos, N. A. Articulation and Growth of Skeletal Elements in Balanid Barnacles (Balanidae, Balanomorpha, Cirripedia). *Royal Society Open Science* **2019**, *6* (9), 190458. https://doi.org/10.1098/rsos.190458.

(39) Newman, W. A.; Zullo, V. A.; Withers, T. H. Cirripedia. In *Treatise on Invertebrate Paleontology*; Part R, Arthropoda; Moore, R. C. Ed., Geological Society of America and Kansas University Press: Lawrence, KS, 1969; Vol. 4(1), pp R206–R295.

(40) Anderson, D. T. *Barnacles: Structure, Function, Development and Evolution*, Chapman&Hall : London, 1994.

(41) DeVol, R. T.; Sun, C.-Y.; Marcus, M. A.; Coppersmith, S. N.; Myneni, S. C. B.; Gilbert, P. U. P. A. Nanoscale Transforming Mineral Phases in Fresh Nacre. *J. Am. Chem. Soc.* **2015**, *137* (41), 13325–13333. https://doi.org/10.1021/jacs.5b07931.

(42) Brandes, J. A.; Wirick, S.; Jacobsen, C. Carbon K-Edge Spectra of Carbonate Minerals. *J Synchrotron Rad* **2010**, *17* (5), 676–682. https://doi.org/10.1107/S0909049510020029.

(43) Cosmidis, J.; Benzerara, K.; Nassif, N.; Tyliszczak, T.; Bourdelle, F. Characterization of Ca-Phosphate Biological Materials by Scanning Transmission X-Ray Microscopy (STXM) at the Ca L2,3-, P L2,3- and C K-Edges. *Acta Biomater* **2015**, *12*, 260–269. https://doi.org/10.1016/j.actbio.2014.10.003.

(44) Nitiputri, K.; Ramasse, Q. M.; Autefage, H.; McGilvery, C. M.; Boonrungsiman, S.; Evans, N. D.; Stevens, M. M.; Porter, A. E. Nanoanalytical Electron Microscopy Reveals a Sequential Mineralization Process Involving Carbonate-Containing Amorphous Precursors. *ACS Nano* **2016**, *10* (7), 6826–6835. https://doi.org/10.1021/acsnano.6b02443.

(45) Kłosowski, M. M.; Friederichs, R. J.; Nichol, R.; Antolin, N.; Carzaniga, R.; Windl, W.; Best, S. M.; Shefelbine, S. J.; McComb, D. W.; Porter, A. E. Probing Carbonate in Bone Forming Minerals on the Nanometre Scale. *Acta Biomaterialia* **2015**, *20*, 129–139. https://doi.org/10.1016/j.actbio.2015.03.039.

(46) Kim, E.; Agarwal, S.; Kim, N.; Hage, F. S.; Leonardo, V.; Gelmi, A.; Stevens, M. M. Bioinspired Fabrication of DNA–Inorganic Hybrid Composites Using Synthetic DNA. *ACS Nano* **2019**, *13* (3), 2888–2900. https://doi.org/10.1021/acsnano.8b06492.

(47) Lawrence, J. R.; Swerhone, G. D. W.; Leppard, G. G.; Araki, T.; Zhang, X.; West, M. M.; Hitchcock, A. P. Scanning Transmission X-Ray, Laser Scanning, and Transmission Electron Microscopy Mapping of the Exopolymeric Matrix of Microbial Biofilms. *Appl Environ Microbiol* **2003**, *69* (9), 5543–5554. https://doi.org/10.1128/AEM.69.9.5543-5554.2003.

(48) DeVol, R. T.; Metzler, R. A.; Kabalah-Amitai, L.; Pokroy, B.; Politi, Y.; Gal, A.; Addadi, L.; Weiner, S.; Fernandez-Martinez, A.; Demichelis, R.; Gale, J. D.; Ihli, J.; Meldrum, F. C.; Blonsky, A. Z.; Killian, C. E.; Salling, C. B.; Young, A. T.; Marcus, M. A.; Scholl, A.; Doran, A.; Jenkins, C.; Bechtel, H. A.; Gilbert, P. U. P. A. Oxygen Spectroscopy and Polarization-Dependent Imaging Contrast (PIC)-Mapping of Calcium Carbonate Minerals and Biominerals. *J. Phys. Chem. B* **2014**, *118* (28), 8449–8457. https://doi.org/10.1021/jp503700g.

(49) Gong, Y. U. T.; Killian, C. E.; Olson, I. C.; Appathurai, N. P.; Amasino, A. L.; Martin, M. C.; Holt, L. J.; Wilt, F. H.; Gilbert, P. U. P. A. Phase Transitions in Biogenic Amorphous Calcium Carbonate. *Proc Natl Acad Sci U S A* **2012**, *109* (16), 6088–6093. https://doi.org/10.1073/pnas.1118085109.
(50) Benzerara, K.; Yoon, T. H.; Tyliszczak, T.; Constantz, B.; Spormann, A. M.; Brown Jr, G. E. Scanning Transmission X-Ray Microscopy Study of Microbial Calcification. *Geobiology* **2004**, *2* (4), 249–259. https://doi.org/10.1111/j.1472-4677.2004.00039.x.
(51) Tsao, C.; Yu, P.-T.; Lo, C.-H.; Chang, C.-K.; Wang, C.-H.; Yang, Y.-W.; Chan, J. C. C. Anhydrous Amorphous Calcium Carbonate (ACC) Is Structurally Different from the Transient Phase of Biogenic ACC. *Chem. Commun.* **2019**, *55* (48), 6946–6949. https://doi.org/10.1039/C9CC00518H.
(52) Xu, Y.; Tijssen, K. C. H.; Bomans, P. H. H.; Akiva, A.; Friedrich, H.; Kentgens, A. P. M.; Sommerdijk, N. A. J. M. Microscopic Structure of the Polymer-Induced Liquid Precursor for Calcium Carbonate. *Nat Commun* **2018**, *9* (1), 2582. https://doi.org/10.1038/s41467-018-05006-w.
(53) Gebauer, D.; Cölfen, H. Prenucleation Clusters and Non-Classical Nucleation. *Nano Today* **2011**, *6* (6), 564–584. https://doi.org/10.1016/j.nantod.2011.10.005.
(54) Albéric, M.; Zolotoyabko, E.; Spaeker, O.; Li, C.; Tadayon, M.; Schmitt, C. N. Z.; Politi, Y.; Bertinetti, L.; Fratzl, P. Heat-Mediated Micro- and Nano-Pore Evolution in Sea Urchin Biominerals. *Crystal Growth & Design* **2022**, *22* (6), 3727–3739. https://doi.org/10.1021/acs.cgd.2c00083.
(55) Nakahara, H. Nacre Formation in Bivalve and Gastropod Molluscs. In *Mechanisms and Phylogeny of Mineralization in Biological Systems*; Suga, S., Nakahara, H., Eds.; Springer Japan: Tokyo, 1991; pp 343–350. https://doi.org/10.1007/978-4-431-68132-8_55.
(56) Checa, A. G.; Salas, C.; Harper, E. M.; Bueno-Pérez, J. de D. Early Stage Biomineralization in the Periostracum of the 'Living Fossil' Bivalve *Neotrigonia*. *PLOS ONE* **2014**, *9* (2), e90033. https://doi.org/10.1371/journal.pone.0090033.
(57) Checa, A. G.; Cartwright, J. H. E.; Willinger, M.-G. Mineral Bridges in Nacre. *Journal of Structural Biology* **2011**, *176* (3), 330–339. https://doi.org/10.1016/j.jsb.2011.09.011.
(58) Messier, R.; Yehoda, J. E. Geometry of Thin-film Morphology. *Journal of Applied Physics* **1985**, *58* (10), 3739–3746. https://doi.org/10.1063/1.335639.
(59) Mullin, J. W. *Crystallization*; Butterworth Heineman: Oxford, 2001.
(60) A. Estroff, L.; Addadi, L.; Weiner, S.; D. Hamilton, A. An Organic Hydrogel as a Matrix for the Growth of Calcite Crystals. *Organic & Biomolecular Chemistry* **2004**, *2* (1), 137–141. https://doi.org/10.1039/B309731E.
(61) Jeanguillaume, C.; Colliex, C.; Ballongue, P.; Teneé, M. New STEM Multisignal Imaging Modes, Made Accessible through the Evaluation of Detection Efficiencies. *Ultramicroscopy* **1992**, *45* (2), 205–217. https://doi.org/10.1016/0304-3991(92)90510-Q.

For Table of Contents Only